JOURNAL OF THE AMERICAN CHEMICAL SOCIETY

pubs.acs.org/JACS

Article

Discovering Targetable Conformation of RhoA Mutant by Integrating Native Mass Spectrometry, Ultraviolet Photodissociation, and X-ray Diffraction

Haozhe Wu,[#] Zheyi Liu,[#] Hao Jiang,[#] Heng Zhao, Chen Dong, Yu Lu, Shijia Zu, Yongjie Guo, Can Lai, Pan Luo, Ke Xu, Yuxin Yang, Yafang Yang, Zhongya Sun, Qingcheng Huang, Huan Xiong, Lanxin Zhou, Yipan Luo, Yuhan Zeng, Daohai Du, Zhongjie Liang, Weilie Xiao, Shan Zhao, Weiqing Zhang, Yong Tang, Chunlei Xiao, Kaixian Chen, Xueming Yang, Fangjun Wang,* and Cheng Luo*

Cite This: *J. Am. Chem. Soc.* 2026, 148, 11709−11718

Read Online

ABSTRACT: Pathogenic mutations in "undruggable" Ras superfamily proteins challenge drug development by inducing subtle, dynamic conformational changes. Here, we integrated X-ray crystallography with native mass spectrometry and ultraviolet photodissociation (nMS-UVPD) to reveal a cryptic conformation in the oncogenic Y42C mutant of RhoA. While crystallography alone resolved two ambiguous structures, nMS-UVPD determined the dominant conformation by directly mapping the mutant's conformational dynamics, identifying an enhanced Mg^{2+}-locked conformation. We explored the mechanism of mutation impairing GTP hydrolysis. This state unmasks a previously hidden, druggable pocket adjacent to Cys42, guiding our identification of a covalent inhibitor. Our integrated approach establishes a roadmap for targeting pathogenic protein mutants previously considered "undruggable" due to their highly dynamic nature.

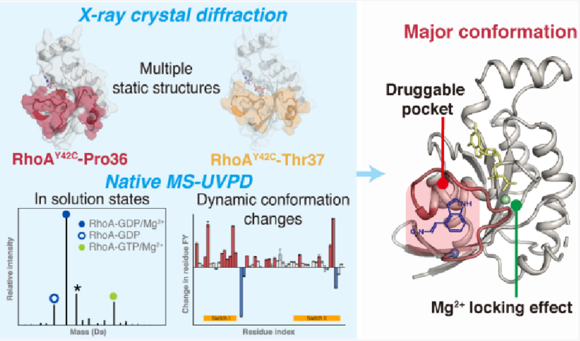

1. INTRODUCTION

The Ras superfamily represents a class of pivotal molecular switches that control fundamental cellular processes. Their aberrant activity is a hallmark of numerous human cancers, making them prime targets for therapeutic intervention.[1] However, these proteins have long been deemed "undruggable" due to their intrinsically dynamic nature and lack of well-defined binding pockets, posing a significant challenge to drug discovery.[2] This therapeutic hurdle is also prominent for cancers driven by specific Ras homologue family member A (RhoA) mutations, such as the Tyr42Cys (Y42C) variant frequently found in diffuse gastric cancer (DGC).[3]

RhoA functions as a molecular switch by cycling between an inactive GDP-bound state and an active GTP-bound state.[4] The nucleotide exchange is facilitated by Rho guanine nucleotide exchange factors (RhoGEFs),[5,6] whereas GTP hydrolysis is catalyzed by Rho GTPase-activating proteins (RhoGAPs).[6] In the cytosol, RhoA is associated with Rho guanine nucleotide dissociation inhibitors (RhoGDIs) and maintained in an inactive state.[7] In addition to GDP/GTP, RhoA requires magnesium ions (Mg^{2+}) as an essential cofactor. Mg^{2+} ion adopts an octahedral coordination geometry formed by six ligands, including phosphate oxygen atoms of the bound nucleotide, the hydroxyl side chain of Thr19, the backbone carbonyl oxygen of Thr37, and two/three coordinating water molecules.[8,9]

As a gain-of-function driver in DGC, the Y42C mutation impairs GTP hydrolysis, enhances ROCK1 interaction and FAK activation,[10] and promotes immunosuppressive remodeling of the tumor microenvironment by conferring a metabolic advantage to regulatory T cells.[11] Moreover, loss of Tyr42 phosphorylation enables Y42C RhoA to evade ubiquitin-mediated degradation, resulting in aberrant protein accumulation and sustained oncogenic signaling.[12] Despite its established role as an oncogenic driver, the molecular mechanism of the Y42C mutant remains an outstanding question. Located distally from the canonical effector region switch I,[13] Y42C mutation is hypothesized to exert its pathogenic effects by subtly altering the protein's conformational landscape. The central challenge is that such dynamic perturbations are often invisible to conventional structural

Received: November 11, 2025
Revised: March 3, 2026
Accepted: March 5, 2026
Published: March 16, 2026

https://doi.org/10.1021/jacs.5c20067

methods such as X-ray crystallography, which may trap nonphysiological states or fail to capture the predominant conformation in solution. A comprehensive understanding therefore demands a multipronged approach that integrates structural snapshots with solution-phase dynamics.

Native mass spectrometry (nMS) is a powerful approach for probing structural dynamics in solution, providing an essential complement to static, solid-state methods.[14] When integrated with MS activation techniques, nMS can yield complementary information on protein stability, topology, and stoichiometry.[15] Among these, 193 nm ultraviolet photodissociation (UVPD) is particularly notable for its ability to induce extensive backbone fragmentation while preserving noncovalent interactions that define the protein fold.[16] The resulting fragmentation patterns serve as high-resolution fingerprints of conformational dynamics, where site-specific fragmentation yields reflect the local structural flexibility. This capability enables precise mapping of interaction and stability changes at single-residue resolution, offering unique advantages for characterizing subtle perturbations in mutant proteins.[17,18]

Herein, we integrated nMS, 193 nm UVPD, and X-ray crystallography to systematically dissect the subtle conformational dynamics induced by the pathogenic Y42C mutation (Figure 1). We resolved two crystallographic structures of GDP-bound Y42C mutants with distinct coordination modes of Mg^{2+}. Through nMS and UVPD analysis, we identified the predominant conformation within dynamic ensembles in solution. Based on these observations, we proposed an enhanced Mg^{2+} locking effect. We further elucidated the mechanism by which the Y42C mutation impairs GTP hydrolysis at the molecular level. Structural comparisons also revealed a specific druggable pocket for the Y42C mutant, within which we successfully identified a covalent inhibitor.

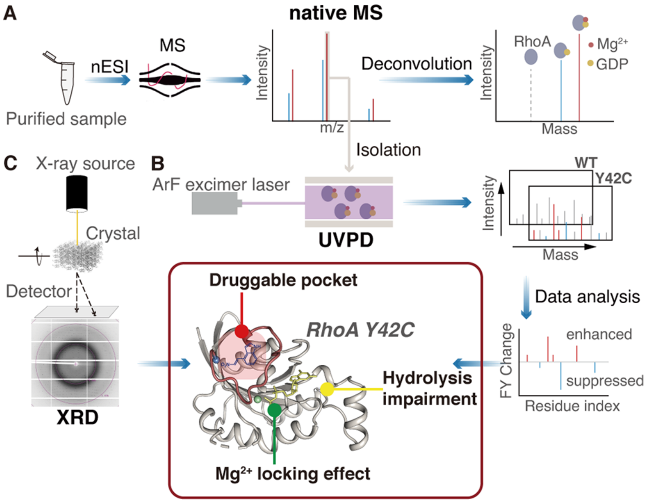

Figure 1. Schematic diagram of workflow to interrogate the RhoA subtle conformational dynamics induced by single amino acid mutation, including (A) native mass spectrometry, (B) 193 nm ultraviolet photodissociation, and (C) X-ray crystal diffraction.

2. RESULTS AND DISCUSSION

2.1. Higher Mg^{2+} Binding Affinity of $RhoA^{Y42C}$ Mutant

Given that RhoA typically cycles between GDP- and GTP-bound states *in vivo*, we first utilized nMS to characterize the wild type (WT) and Y42C mutant of RhoA expressed in *E. coli*. The nMS analysis revealed that $RhoA^{Y42C}$-GDP/Mg^{2+} complex exhibited a narrow charge state distribution (CSD) nearly identical to that of the WT (Figure 2A), indicating a preserved global fold.[19] Specifically, both Mg^{2+}-free (RhoA-GDP) and Mg^{2+}-bound (RhoA-GDP-Mg^{2+}) species were resolved in the spectra. However, the relative abundance of RhoA-GDP to RhoA-GDP-Mg^{2+} was significantly lower in the Y42C mutant compared to that in the WT (Figure 2B), suggesting increased affinity for Mg^{2+} induced by the Y42C mutation. Furthermore, the GTP-bound form of RhoA was also detected in the purified RhoA samples, consistent with previous nMS analysis of other GTPases such as KRAS.[20] However, a striking difference in the relative abundance of the GTP-bound species was observed between the Y42C mutant and the WT. The GTP-bound form was prominent in the Y42C samples but substantially less abundant in the WT samples (Figure 2B). This difference implies an impaired intrinsic GTPase hydrolysis activity induced by the mutation, thereby allowing the Y42C mutant to preferentially retain the co-purified GTP form.

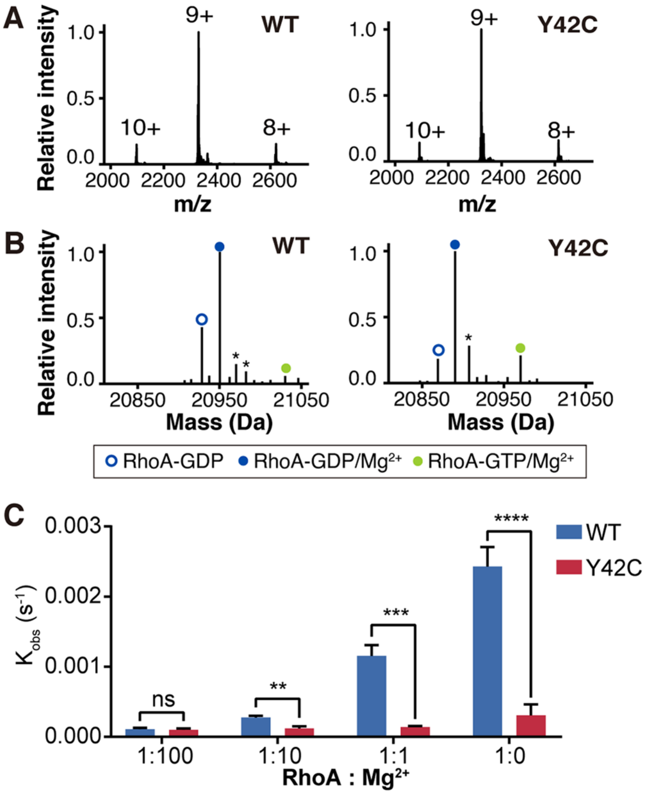

Figure 2. Enhanced Mg^{2+} locking effect of $RhoA^{Y42C}$ mutant. (A) nMS spectra of RhoA samples in 200 mM NH_4Ac; (B) deconvoluted spectra of nMS spectra shown in panel A. The different forms of RhoA were labeled. Asterisks denote sodium-, potassium-, and ammonium-bound adducts. (C) Comparison of endogenous GDP release rates at different Mg^{2+} concentrations. GDP release rates were determined using MANT-GDP, based on the fluorescence decrease upon MANT-GDP dissociation. The K_{obs} values for $RhoA^{WT}$/$RhoA^{Y42C}$ are $2.4 \times 10^{-3}/3.0 \times 10^{-4}$ s^{-1} (1:0), $1.2 \times 10^{-3}/1.4 \times 10^{-4}$ s^{-1} (1:1), $2.8 \times 10^{-4}/1.2 \times 10^{-4}$ s^{-1} (1:10), and $1.1 \times 10^{-4}/1.0 \times 10^{-4}$ s^{-1} (1:100). Data are mean ± SD (n = 3 biologically independent experiments). Significant differences were observed for RhoA:Mg^{2+} = 1:0 ($P = 0.0003$), RhoA:Mg^{2+} = 1:1 ($P = 0.0004$), and RhoA:Mg^{2+} = 1:10 ($P = 0.0025$), whereas RhoA:Mg^{2+} = 1:100 ($P = 0.6445$) showed no significant difference. Two-sided unpaired *t* test (threshold, $\alpha = 0.05$).

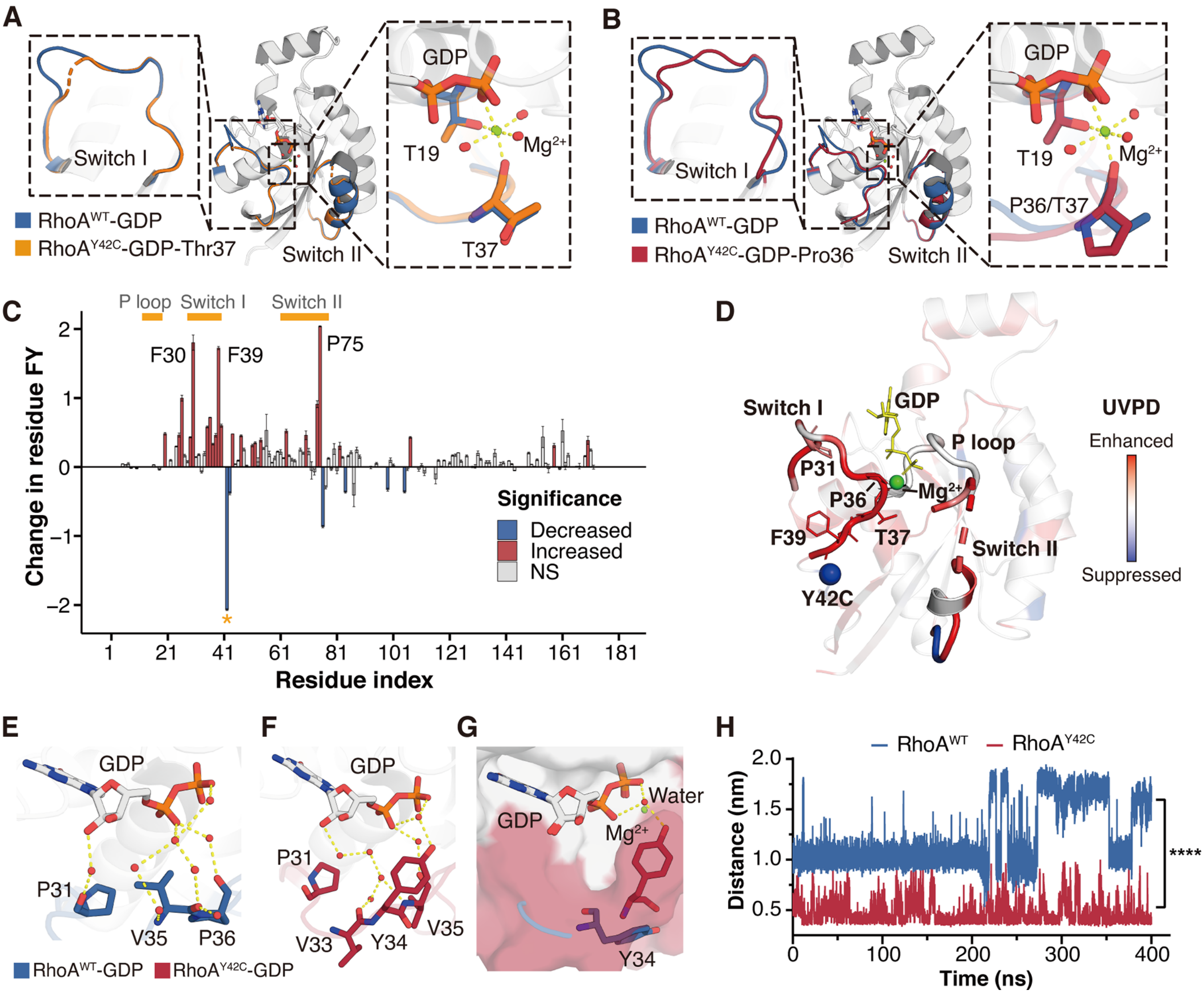

Figure 3. Dynamic conformation of GDP-bound RhoA^{Y42C} mutant. (A) Superposition of crystal structures of RhoA^{Y42C}-GDP-Thr37 (PDB code: 9VNI, orange) and RhoA^{WT}-GDP (PDB code: 9VNH, blue), exhibiting similar Switch I motif and Mg^{2+} coordination. (B) Superposition of crystal structures of RhoA^{Y42C}-GDP-Pro36 (PDB code: 8ZNY, red) and RhoA^{WT}-GDP (PDB code: 9VNH, blue), exhibiting significant differences in Switch I motif and Mg^{2+} coordination. (C) Changes in residue FY (ΔFYs) in UVPD analysis induced by Y42C mutation. The significance threshold was set at $p < 0.01$ and $|\Delta FY| \geq 0.3$. The yellow asterisk denotes the mutation site (Y42C). (D) Structural mapping of UVPD FY changes on the RhoA^{Y42C}-GDP/Mg^{2+} complex. The structure is colored based on the FY changes, where red indicates enhanced fragmentation and blue indicates suppressed fragmentation in the mutant. (E) Water bridges between Switch I and GDP in the WT structure. Distance of annotated hydrogen bonds is between 2.4 and 3.4 Å. (F) Water bridges between Switch I and GDP in the Y42C mutant structure. Distance of annotated hydrogen bonds is between 2.5 and 3.2 Å. (G) Interaction details between Tyr34 and Mg^{2+}. Tyr34 interacted more strongly with α, β-phosphate of GDP through a water molecule in RhoA^{Y42C}. (H) Distance between oxygen of Tyr34 side chain and Mg^{2+} in molecular dynamics simulation, with 1.209 nm in RhoA^{WT} compared to 0.459 nm in RhoA^{Y42C} in average. Significant differences were observed with $P < 0.0001$. Data are mean ± SD (n = 40001 during molecular dynamics simulation trajectories). Two-sided unpaired t test (threshold, $\alpha = 0.05$).

Thus, we investigated substrate dissociation kinetics using a *N*-methyl-anthraniloyl-GDP (MANT-GDP) fluorescence assay under different Mg^{2+} concentrations, since exchanging Mg^{2+} with the surrounding milieu is known to promote GDP release.[21] As the concentration of Mg^{2+} decreased, RhoA^{WT} exhibited progressively accelerated dissociation of MANT-GDP (Figure 2C and Figure S1A). In contrast, while RhoA^{Y42C} showed a comparable release rate to WT at high Mg^{2+} concentrations, its GDP dissociation was significantly slower than that of WT under low Mg^{2+} conditions, consistent with enhanced Mg^{2+} binding observed by nMS. Collectively, the Y42C mutation confers increased Mg^{2+} affinity for RhoA, thereby stabilizing the nucleotide binding pocket and reducing substrate release under Mg^{2+}-limiting environments.

2.2. Mg^{2+} Locking Effect in Dynamic RhoA Cycling Conformations

To investigate the structural basis for the enhanced Mg^{2+} affinity, we determined the crystal structures of both WT and Y42C mutant proteins (Table S1). The crystal structure of WT closely resembles a previously reported stabilizing mutant, Phe25Asn,[8] with a root-mean-square deviation (RMSD) of 1.193 Å (with major differences in Switch II; Figure S2A−C). Remarkably, we resolved two distinct conformations of the Y42C mutant. One form is nearly identical to the WT structure

(RMSD = 0.674 Å), where the backbone carbonyl of Thr37 coordinates Mg^{2+} (Figure 3A and Figure S2D,E). In contrast, the second form adopts a different conformation in which Mg^{2+} is coordinated by the backbone carbonyl of Pro36, resulting in a greater deviation from the WT structure (RMSD = 1.685 Å; Figure 3B and Figure S2F,G). The presence of two distinct conformational states in the crystal structures indicates the conformational heterogeneity of the Y42C mutant. However, static crystallographic snapshots alone are insufficient to determine which conformation predominates in solution.

Thus, we further investigated changes of conformation dynamics induced by Y42C mutation by using nMS coupled with 193 nm UVPD (Figures S3A,B and S4), which directly interrogates the conformation dynamics of the protein in the solution phase. In UVPD analysis, alterations in residue fragmentation yields (FYs) serve as informative proxies for local structural flexibility, where changes can indicate altered local interactions.[17,22] Besides, residue properties also influence FYs.[23] The comparable FY profiles of WT and Y42C mutants indicate they share overall similar conformations (Figure S3C), consistent with the X-ray crystallography results. A significant FY decrease was observed at the mutation site (Figure 3C and Figure S3D), primarily attributed to the difference in photon absorption between tyrosine and cysteine. Through examining the changes in residue FYs, a general increase in FYs across the Switch II region (residues 61−78) was observed for the Y42C mutant (Figure 3C−D), indicating enhanced conformational flexibility. This observation is consistent with the above-mentioned X-ray crystallography results, which showed substantial disorder in Switch II in both Y42C crystal structures (Figure 3A,B and Figure S2E,G). A marked increase in FYs in the region spanning Pro36 to Phe39 was observed in the Y42C mutant compared to the WT (Figure 3C−D), indicating significant local destabilization. As reported previously,[8,24−26] coordination of Pro36/Thr37 with Mg^{2+} directly affects the stability of Phe39 (Figure S5A,B). Our crystal structures show that only in the Pro36-coordinated state does the Phe39 side chain flip outward, losing stabilizing interactions with Ile23 and becoming highly flexible (Figure S5C,D). Further, the backbone carbonyl of Pro31 forms a water bridge to the ribose hydroxyl of GDP in $RhoA^{WT}$ (Figure 3E and Figure S5E). Although the Thr37-coordinated Y42C structure shares a similar interaction with WT (Figure S4F,G), this water bridge is absent in the Pro36-coordinated Y42C structure (Figure 3F and Figure S5H). Additionally, $RhoA^{WT}$ exhibits a more intricate hydration network around Pro36 compared to the Y42C mutant (Figure 3E,F). Thus, converging evidence from X-ray crystallography and UVPD supports the Pro36-coordinated conformation as a major solution-relevant structural state of the Y42C mutant.

Based on this preferred conformation, we elucidated the molecular basis for enhanced Mg^{2+} binding. A key feature of this state is a novel water-mediated interaction between the side chain of Tyr34 and the α, β-phosphates of GDP (Figure 3G). We hypothesized that this Tyr34-GDP bridge acts as a 'latch' to better secure the Mg^{2+}. This model was supported by a 400 ns molecular dynamics (MD) simulation, which confirmed a significantly shorter and more stable distance between the Tyr34 hydroxyl group and Mg^{2+} in the Y42C mutant compared to WT (Figure 3H and Figure S5I). In addition, the dynamic differences in the Switch regions between the Y42C mutant and WT were also observed in MD simulation (Figure S5J), consistent with the observation of UVPD.

We further found that this novel "Mg^{2+}-locked" state in Y42C mutant hinders GDP release, thereby impairing the kinetics of GDP/GTP exchange. We compared the GDP/GTP exchange rates between $RhoA^{WT}$ and $RhoA^{Y42C}$ in the presence of EDTA, a Mg^{2+} chelator. Consistent with the reduced substrate release rate resulting from enhanced Mg^{2+} binding, the Y42C mutation significantly impaired the GDP/GTP exchange rate of RhoA (Figure S5K). Additionally, the Y42C mutation markedly inhibited GDP/GTP exchange catalyzed by the DH-PH domain of RhoGEF Dbs under Mg^{2+}-deficient conditions (Figure S5L), further underscoring the mutation's disruptive effect on nucleotide cycling.

2.3. High Binding Affinity of Mg^{2+} Causing a Lower Cycling Rate

In the GDP-bound state, RhoGDIs inhibit RhoA activity and stabilize C-terminal hydrophobic modification of RhoA by binding to Switch I and Switch II regions.[7] The structural changes we observed in the Y42C mutant, including the outward flip of Phe39 in Switch I and increased flexibility in Switch II suggested that its interaction with RhoGDI might be altered (Figure S6A,B). Thus, we investigated this interaction using nMS and revealed a Mg^{2+}-dependent interaction between RhoA and RhoGDI1, with binding occurring exclusively in the RhoA-GDP/Mg^{2+} state (Figure S6C). Consistent with the enhanced Mg^{2+} binding observed in the Y42C mutant, the Y42C mutant formed a more stable complex with RhoGDI1 than the WT (Figure S6C). This strengthened interaction was further validated by both *in vitro* pull-down assay (Figure S6D) and co-immunoprecipitation assay (Figure S6E).

Functionally, the increased affinity between $RhoA^{Y42C}$ and RhoGDI1 attenuated the substrate exchange rate catalyzed by RhoGEF in the presence of RhoGDI1 (Figure S6F). Furthermore, we reconstituted the entire RhoA nucleotide cycle *in vitro*, including RhoGEF LARG, RhoGDI1, and RhoGAP p50GAP. In this system, the Y42C mutant had a reduced overall rate of GTP hydrolysis, confirming the entire cycle is slower (Figure S6G). Collectively, these results suggest that enhanced interaction with RhoGDI1 contributes to a reduced effective GDP/GTP exchange rate for the Y42C. Such a compensatory effect may partially offset the impaired GTP hydrolysis of Y42C, providing a mechanistic framework for why cellular GTP-bound RhoA levels in the Y42C mutant do not increase dramatically relative to wild type, as reported previously.[10]

2.4. Destabilization of GTP-Binding Pocket Impairs Hydrolysis

We next investigated the impact of the Y42C mutation on RhoA in the active GTP-bound state. To exclude the influence of GTP hydrolysis, we used the nonhydrolyzable analogue GMPPNP as a substitute. Unlike the GDP-bound form, nMS did not reveal pronounced differences in the binding of magnesium ions (Figure S7A). Notably, UVPD provided further structural insights (Figure S7B−D). Compared with the GDP-bound state, Switch I had a similar FYs increase when bound with GMPPNP (Figure S8A). Consistently, crystallography revealed a substantial conformational change in Switch I (RMSD = 1.736 Å; Figure S8B−D and Table S1). As in GDP-bound form, $RhoA^{Y42C}$ coordinated Mg^{2+} via the Pro36 backbone carbonyl rather than the Thr37 side chain hydroxyl.

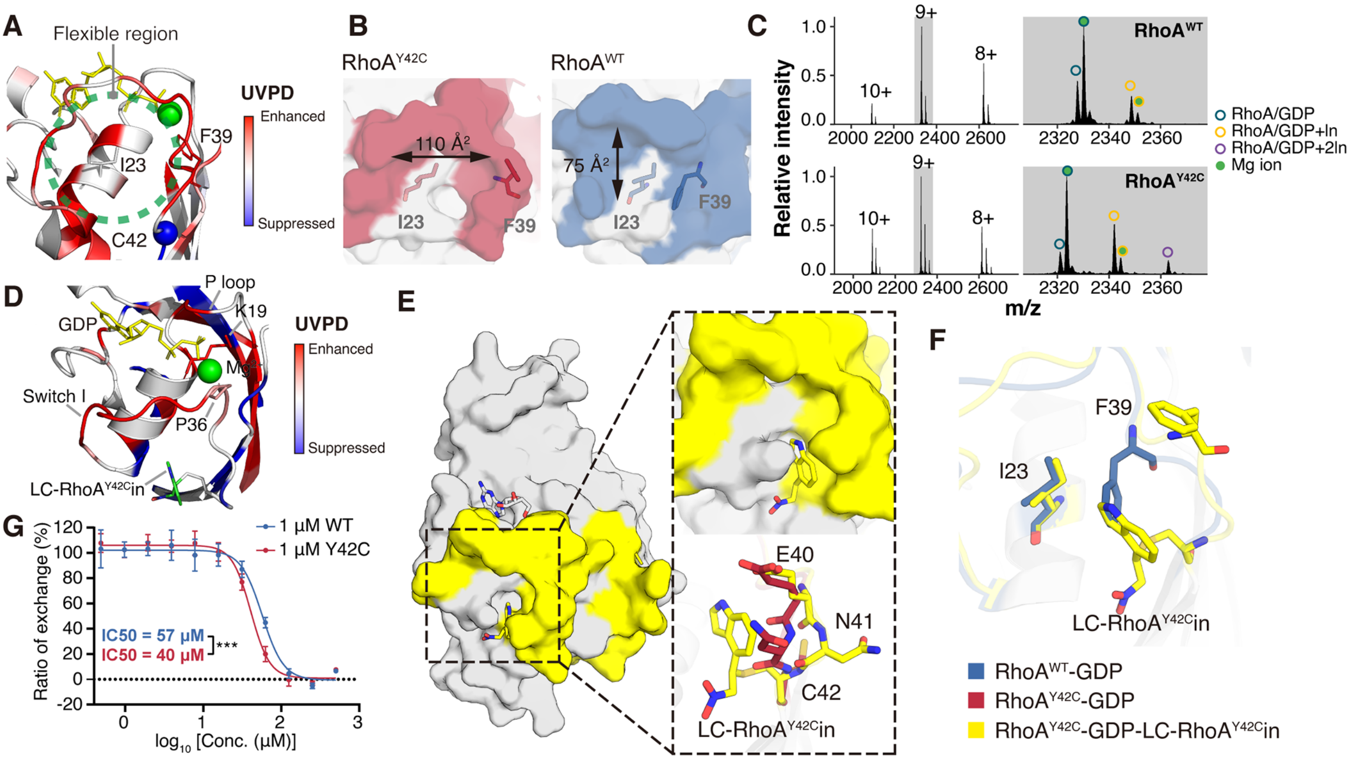

Figure 4. Covalent inhibitor targeting RhoA^{Y42C}. (A) The Cys42/Switch I pocket was indicated by the changes in residue FY. (B) Cys42/Switch I pocket of RhoA^{Y42C}-GDP (left) and inactive form of RhoA^{WT}-GDP (right). (C) nMS analysis of RhoA interaction with LC-RhoA^{Y42C}in. The main peak, corresponding to the 9+ charge state, was selected for analysis. LC-RhoA^{Y42C}in (In) was annotated as a modification. Increased mass due to modification was detected in 23.5% of WT and 41.8% of the Y42C mutant, with a minor fraction carrying two modifications. (D) Changes in residue FY of RhoA^{Y42C} induced by Cys42 modification mapped to the crystal structure of RhoA^{Y42C}. (E) Crystal structure of Y42C mutant and LC-RhoA^{Y42C}in complex, showing Glu40, Asn41, and Cys42 of RhoAY42C-apo (red) or RhoA^{Y42C}-LC-RhoA^{Y42C}in complex (PDB code: 9VNG, yellow). (F) Cys42/Switch I pocket of RhoA^{Y42C}-LC-RhoA^{Y42C}in (yellow) or RhoA^{WT}-GDP (blue). (G) Inhibition of the exchange of RhoA$^{WT/Y42C}$ by LC-RhoA^{Y42C}in. Inhibition was measured based on the fluorescence increase caused by MANT-GDP loading onto RhoA. Concentration of the exchange system: 1 μM RhoA, 2 μM MANT-GDP, 5 mM Mg^{2+}, 10 mM EDTA. IC_{50} of LC-RhoA^{Y42C}in for RhoA^{WT}/RhoA^{Y42C} is 57 ± 4.3/40 ± 1.8 μM. Significant differences were observed with $P = 0.0004$. Data are mean ± SD ($n = 4$ biologically independent experiments). Two-sided unpaired t test (threshold, $\alpha = 0.05$).

In Ras superfamily proteins bound with GTP, Tyr42 (or a homologous site) typically interacts with Asp59 (or a homologous site) either directly or through a bridging water molecule (Figure S8E). Substitution by cysteine abolishes this interaction, leading to shortening of the β-sheet at the C-terminal end of Switch I (Figure S8F,G). As a result, both Switch I and Gln63 exhibited decreased stability, in agreement with UVPD data (Figure S8H).

In the hydrolysis pocket, the conserved water molecule normally stabilized by Gln63 to attack γ-phosphate was absent in RhoA^{Y42C}, as no electron density could be detected (Figure S8I,J). Together, these perturbations markedly impair the hydrolytic capacity of the Y42C mutant (Figure S8K). To directly assess the functional consequence of these structural perturbations in a dynamic context, intrinsic GTPase activity was also evaluated by nMS.[20] Whereas WT underwent rapid intrinsic GTP hydrolysis, the Y42C mutant exhibited a pronounced reduction in catalytic activity, retaining a greater GTP-bound population over the course of the experiment (Figure S8L). These data are consistent with the disrupted hydrolysis pocket observed crystallographically, indicating impaired intrinsic GTP hydrolysis in the Y42C mutant.

2.5. Unique RhoA^{Y42C} Switch I Dynamics Make Selective Targeting Possible

The constitutive alteration of the octahedral coordination geometry centered on Mg^{2+} substantially affects the interactions among its surrounding residues, thereby inducing unique conformational dynamics within the Switch I region. Crucially, this structural rearrangement creates an opportunity for the selective inhibition of the Y42C mutant. The disruption of the hydrophobic interaction between Phe39 and Ile23, combined with the smaller side chain of cysteine relative to tyrosine, generates a highly flexible region adjacent to Cys42, as revealed by 193 nm UVPD analysis (Figure 4A). This observation suggests an expansion of the local structural environment around Cys42 in three-dimensional space, which is corroborated by crystallographic data (Figure 4B). Drawing inspiration from the successful development of covalent inhibitors targeting the highly reactive cysteine in KRAS^{G12C} mutant,[27] we sought to explore whether a similar mutant-selective strategy could be applied to RhoA^{Y42C}. In this context, the newly formed pocket in RhoA^{Y42C}, termed the Cys42/Switch I pocket, emerges as a potential site for the development of mutant-selective inhibitors.

Subsequently, we conducted a fragment-based covalent inhibitor screen targeting reactive Cys (Figure S9A and Table S2), resulting in the identification of a covalent inhibitor, termed LC-RhoA^{Y42C}in (Figure S9B and Table S2, B10 differs only in its modification site, and the more active B11 was chosen for further study). Featuring a nitroethylene warhead, LC-RhoA^{Y42C}in engages in a Michael addition reaction with the cysteine thiol, forming a stable covalent adduct (Figure S9C). The selectivity of LC-RhoA^{Y42C}in toward the Y42C mutant was evaluated by nMS. Upon incubation at a 1:4 molar ratio for 2 h, LC-RhoA^{Y42C}in exhibited higher covalent modification efficiency of the Y42C mutant (41.8%) relative to WT (23.5%) (Figure 4C). Further UVPD sequence analysis of the covalently modified RhoA^{Y42C} confirmed Cys42 as the primary modification site, whereas in the WT, the compound was found to primarily engage Cys20 (Figure 4D and Figure S9D,E). Intriguingly, nMS revealed an increased relative abundance of RhoA^{Y42C}-GDP compared to the RhoA^{Y42C}-GDP/Mg^{2+} complex upon inhibitor binding (Figure 4C), indicative of diminished Mg^{2+} stability. This finding aligns with the elevated flexibility observed in the P-loop region by 193 nm UVPD (Figure 4D and Figure S9F), suggesting that LC-RhoA^{Y42C}in binding induces dynamic conformational changes that partially alleviate the Mg^{2+}-mediated conformational lock. Consistently, crystallographic data show that binding of LC-RhoA^{Y42C}in to Cys42 induces displacement of the Switch I terminus (Figure 4E, S9G,H and Table S1), with the indole ring oriented toward the hydrophobic pocket region (Figure 4F). Functional assays demonstrated that LC-RhoA^{Y42C}in inhibited RhoA nucleotide exchange in a dose-dependent manner, with an IC$_{50}$ lower for the Y42C mutant compared to WT (Figure 4G and Figure S9I), confirming its selective inhibitory potency.

Furthermore, we identified a potential allosteric pocket in active RhoA^{Y42C} that closely resembles the Switch I/II (SI/II) pocket previously described in Kras mutants.[28] This pocket was not observed in RhoA^{WT}. Moreover, UVPD analysis revealed significant changes in FYs for residues surrounding the SI/II pocket (Figure 5A), which is consistent with the increased conformational flexibility of both the Switch I and Switch II regions induced by this mutation (Figure S5I). These differences were corroborated by MD simulations, which indicated pronounced conformational divergence in this region between RhoA^{WT} and RhoA^{Y42C} (Figure S10A,B). Quantitative analysis revealed that the SI/II pocket in RhoA^{Y42C} exhibited markedly increased volume and average solvent-accessible surface area (461.1 Å^3 and 303.5 Å^2, respectively) compared to RhoA^{WT} (198.5 Å^3 and 125.9 Å^2) (Figure S10C,D), suggesting the emergence of a mutant-specific pocket. Structural alignment of the lowest energy conformation of RhoA^{Y42C} (from MD simulation) with the crystal structure of Kras^{G12D}-GDP complex bound to the allosteric inhibitor BI-2852 revealed a spatial resemblance (Figure 5B,C). This observation implies that the SI/II pocket of RhoA^{Y42C} may serve as an additional site for therapeutic targeting, in agreement with prior studies reporting allosteric compounds interacting with RhoA at Trp58.[29]

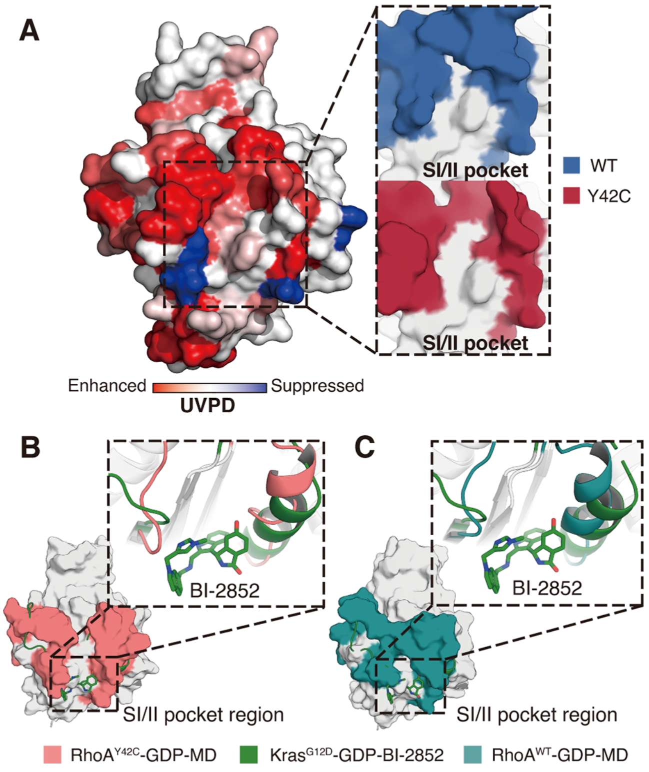

Figure 5. Potential pocket for selectively targeting RhoA^{Y42C}. (A) SI/II pocket colored with changes in residue FY and the SI/II pocket of RhoA. (B) Superposition of the lowest energy conformation of GDP-bound RhoA^{Y42C} and Kras^{G12D} bound with GDP and BI-2852 (PDB 6ZL5, green). (C) Superposition of the lowest energy conformation of GDP-bound RhoA^{WT} and Kras^{G12D} bound with GDP and BI-2852 (PDB code: 6ZL5, green).

2.6. Discussion

Interrogating the subtle conformational dynamics of Ras superfamily proteins is challenging, especially for the single-point mutants. Minor changes can disrupt the normal conformation of Switch I/II regions, leading to the instability of the entire protein, further resulting in changes of substrate, regulator, and effector binding capabilities.[30] Although continuous technological innovation has been carried out,[25,31] it is still impossible to fully capture the unique conformational dynamics of single-point mutants of Ras superfamily proteins, making them still "undruggable targets".

In this study, crystallographic analysis resolved two distinct GDP-bound conformations of the Y42C mutant, differing in the coordination mode of cofactor Mg^{2+}. nMS-UVPD further revealed that Pro36-coordinated structure represents the preferred conformation, exhibiting enhanced Mg^{2+}-locking effect and elevated RhoGDI1 binding. Y42C mutant was identified to destabilize the GTP-binding pocket particularly around the γ-phosphate when binding GMPPNP. This led to the loss of a key catalytic water molecule, ultimately impairing the hydrolytic activity of RhoA. This series of results suggests that Y42C mutation may slow down cycling, characterized by impaired GTP hydrolysis and, potentially in cells, by enhanced interaction with RhoGDI leading to reduced GDP/GTP exchange. This is unique because most of the existing RhoA pathogenic mutations cause fast substrate cycles.[26] In addition, the increase in RhoGDI1 association observed for Y42C was markedly weaker in cellular co-immunoprecipitation than in biochemical pull-down assays, suggesting that a fraction of Y42C may preferentially associate with membranes and thereby escape RhoGDI-mediated sequestration, consistent with previous reports of elevated FAK phosphorylation and aberrant downstream signaling in Y42C-expressing cells.[10]

Traditional crystallography provides only static structural information, as illustrated by our observation of two distinct conformations of the Y42C mutant. However, nMS coupled with 193 nm UVPD enables residue-level interrogation of nearly every amino acid, offering rich insights into conformational dynamics, particularly for single-point mutations. For example, UVPD revealed that the Pro36-coordinated state represents the preferred binding mode in solution. Moreover, UVPD captured conformational differences in Switch II, which were unresolved in crystallography due to missing electron density. Because of lattice constraints and the conserved fold of protein, crystallography often overlooks subtle structural variations.

DGC is a highly lethal malignancy with increasing incidence and a poor prognosis. Y42C mutation of RhoA, frequently co-occurring with *CDH1* deletion, has been identified as a key driver in DGC progression.[10] Structural interrogation of RhoA^{Y42C} thus offers a promising avenue to uncover the mechanisms of tumorigenesis and inform therapeutic strategies. In our study, an expanded surface region adjacent to Cys42 was revealed, resulting from weakened hydrophobic packing between Phe39 and Ile23. Exploiting these unique conformational features, we identified a cryptic, mutant-specific pocket and developed a prototype covalent inhibitor (LC-RhoA^{Y42C}in) that targets the Y42C mutant via Michael addition within the Cys42/Switch I pocket. Although LC-RhoA^{Y42C}in exhibits differential activity toward the WT and Y42C variants, this distinction remains insufficient to constitute a true selectivity. Given that LC-RhoA^{Y42C}in is a small electrophilic fragment bearing a highly reactive warhead, its application in cellular systems may be constrained by off-target reactivity. Consequently, further lead optimization will be required to enhance both selectivity and pharmacological properties for potential *in vivo* applications.

3. CONCLUSIONS

In summary, we have elucidated the subtle conformational dynamics of RhoA^{Y42C} by integrating orthogonal structural techniques, including nMS, 193 nm UVPD, and X-ray crystallography. This multidisciplinary approach, combining dynamic and static structural information, has enabled us to unravel the complex mechanisms underlying RhoA^{Y42C} dysfunction and to identify druggable pockets suitable for the development of potential mutation-specific inhibitors targeting diffuse gastric cancer. Although RhoA undergoes multiple post-translational modifications in cells, such as prenylation[7] and phosphorylation,[12,32] which are not captured in the bacterial expression system, these modifications mainly regulate cellular localization and signaling context. The structural and dynamic features identified here thus represent intrinsic properties of the Y42C mutant and provide a molecular framework for subsequent cellular regulation. We note that the high-resolution structural insights provided by this workflow rely on extensive backbone fragmentation coverage, which currently limits its direct application to proteins with a molecular weight below 50 kDa. However, for high-molecular-weight proteins, this limitation can be circumvented by analyzing isolated functional domains, a strategy previously validated in our work.[33] Ultimately, our findings highlight that probing unobvious yet distinctive conformational dynamics is essential for the selective targeting of previously "undruggable" pathogenic mutants, thereby expanding the conventional drug discovery paradigm that relies predominantly on well-defined stable binding sites.

■ ASSOCIATED CONTENT

Supporting Information

The Supporting Information is available free of charge at https://pubs.acs.org/doi/10.1021/jacs.5c20067.

Experimental section; nMS and UVPD of RhoA$^{WT/Y42C}$-GDP, RhoA$^{WT/Y42C}$-GMPPNP, and RhoA$^{WT/Y42C}$-LC-RhoA^{Y42C}in; nMS of RhoA$^{WT/Y42C}$-RhoGDI complex; expanded crystal structure details and electron cloud density; molecular dynamics simulation related data; substrate exchange data and GTP hydrolysis data; pull-down and co-immunoprecipitation data (PDF)

■ AUTHOR INFORMATION

Corresponding Authors

Fangjun Wang − *State Key Laboratory of Chemical Reaction Dynamics, Dalian Institute of Chemical Physics, Chinese Academy of Sciences, Dalian 116023, China; University of Chinese Academy of Sciences, Beijing 100049, China;* orcid.org/0000-0002-8118-7019; Email: wangfj@dicp.ac.cn

Cheng Luo − *State Key Laboratory of Discovery and Utilization of Functional Components in Traditional Chinese Medicine, Guizhou Medical University, Guiyang 561113, China; State Key Laboratory of Drug Research, Shanghai Institute of Materia Medica, Chinese Academy of Sciences, Shanghai 201203, China; University of Chinese Academy of Sciences, Beijing 100049, China; Zhongshan Institute for Drug Discovery, Shanghai Institute of Materia Medica, Chinese Academy of Sciences, Guangdong 528400, China; School of Pharmaceutical Science and Technology, Hangzhou Institute for Advanced Study, University of Chinese Academy of Sciences, Hangzhou 310024, China;* orcid.org/0000-0003-3864-8382; Email: cluo@simm.ac.cn

Authors

Haozhe Wu − *State Key Laboratory of Discovery and Utilization of Functional Components in Traditional Chinese Medicine, Guizhou Medical University, Guiyang 561113, China; State Key Laboratory of Drug Research, Shanghai Institute of Materia Medica, Chinese Academy of Sciences, Shanghai 201203, China; University of Chinese Academy of Sciences, Beijing 100049, China*

Zheyi Liu − *State Key Laboratory of Chemical Reaction Dynamics, Dalian Institute of Chemical Physics, Chinese Academy of Sciences, Dalian 116023, China; University of Chinese Academy of Sciences, Beijing 100049, China*

Hao Jiang − *State Key Laboratory of Drug Research, Shanghai Institute of Materia Medica, Chinese Academy of Sciences, Shanghai 201203, China; University of Chinese Academy of Sciences, Beijing 100049, China*

Heng Zhao − *State Key Laboratory of Chemical Reaction Dynamics, Dalian Institute of Chemical Physics, Chinese Academy of Sciences, Dalian 116023, China*

Chen Dong − *State Key Laboratory of Drug Research, Shanghai Institute of Materia Medica, Chinese Academy of Sciences, Shanghai 201203, China; University of Chinese Academy of Sciences, Beijing 100049, China*

Yu Lu − *School of Life Science and Technology, ShanghaiTech University, Shanghai 200031, China*

Shijia Zu − *State Key Laboratory of Drug Research, Shanghai Institute of Materia Medica, Chinese Academy of Sciences,* *Shanghai 201203, China; University of Chinese Academy of Sciences, Beijing 100049, China; School of pharmacy, Fudan University, Shanghai 201203, China*

Yongjie Guo − *State Key Laboratory of Chemical Reaction Dynamics, Dalian Institute of Chemical Physics, Chinese Academy of Sciences, Dalian 116023, China*

Can Lai − *State Key Laboratory of Chemical Reaction Dynamics, Dalian Institute of Chemical Physics, Chinese Academy of Sciences, Dalian 116023, China; University of Chinese Academy of Sciences, Beijing 100049, China*

Pan Luo − *State Key Laboratory of Chemical Reaction Dynamics, Dalian Institute of Chemical Physics, Chinese Academy of Sciences, Dalian 116023, China*

Ke Xu − *State Key Laboratory of Drug Research, Shanghai Institute of Materia Medica, Chinese Academy of Sciences, Shanghai 201203, China; University of Chinese Academy of Sciences, Beijing 100049, China;* orcid.org/0009-0000-7111-3131

Yuxin Yang − *State Key Laboratory of Drug Research, Shanghai Institute of Materia Medica, Chinese Academy of Sciences, Shanghai 201203, China; University of Chinese Academy of Sciences, Beijing 100049, China*

Yafang Yang − *State Key Laboratory of Drug Research, Shanghai Institute of Materia Medica, Chinese Academy of Sciences, Shanghai 201203, China*

Zhongya Sun − *State Key Laboratory of Drug Research, Shanghai Institute of Materia Medica, Chinese Academy of Sciences, Shanghai 201203, China*

Qingcheng Huang − *State Key Laboratory of Drug Research, Shanghai Institute of Materia Medica, Chinese Academy of Sciences, Shanghai 201203, China; University of Chinese Academy of Sciences, Beijing 100049, China*

Huan Xiong − *State Key Laboratory of Drug Research, Shanghai Institute of Materia Medica, Chinese Academy of Sciences, Shanghai 201203, China; Zhongshan Institute for Drug Discovery, Shanghai Institute of Materia Medica, Chinese Academy of Sciences, Guangdong 528400, China;* orcid.org/0009-0002-8920-9355

Lanxin Zhou − *State Key Laboratory of Discovery and Utilization of Functional Components in Traditional Chinese Medicine, Guizhou Medical University, Guiyang 561113, China; Zhongshan Institute for Drug Discovery, Shanghai Institute of Materia Medica, Chinese Academy of Sciences, Guangdong 528400, China*

Yipan Luo − *Zhongshan Institute for Drug Discovery, Shanghai Institute of Materia Medica, Chinese Academy of Sciences, Guangdong 528400, China; School of Pharmacy, Zunyi Medical University, Zunyi 563000, China*

Yuhan Zeng − *Zhongshan Institute for Drug Discovery, Shanghai Institute of Materia Medica, Chinese Academy of Sciences, Guangdong 528400, China; School of Pharmaceutical Sciences, Southern Medical University, Guangzhou 510515, China*

Daohai Du − *State Key Laboratory of Drug Research, Shanghai Institute of Materia Medica, Chinese Academy of Sciences, Shanghai 201203, China*

Zhongjie Liang − *Center for Systems Biology, Department of Bioinformatics, School of Biology and Basic Medical Sciences, Soochow University, Suzhou 215123, China;* orcid.org/0000-0003-0763-5407

Weilie Xiao − *State Key Laboratory for Conservation and Utilization of Bio-Resources in Yunnan, School of Pharmacy and School of Chemical Science and Technology, Yunnan University, Kunming 650500, China; Southwest United Graduate School, Kunming 650592, China;* orcid.org/0000-0001-6826-1993

Shan Zhao − *State Key Laboratory of Chemical Reaction Dynamics, Dalian Institute of Chemical Physics, Chinese Academy of Sciences, Dalian 116023, China*

Weiqing Zhang − *State Key Laboratory of Chemical Reaction Dynamics, Dalian Institute of Chemical Physics, Chinese Academy of Sciences, Dalian 116023, China; University of Chinese Academy of Sciences, Beijing 100049, China;* orcid.org/0000-0001-6518-4152

Yong Tang − *Ensem Therapeutics, Inc., Medford, Massachusetts 02155, United States*

Chunlei Xiao − *State Key Laboratory of Chemical Reaction Dynamics, Dalian Institute of Chemical Physics, Chinese Academy of Sciences, Dalian 116023, China; University of Chinese Academy of Sciences, Beijing 100049, China;* orcid.org/0000-0002-1549-5945

Kaixian Chen − *State Key Laboratory of Drug Research, Shanghai Institute of Materia Medica, Chinese Academy of Sciences, Shanghai 201203, China; University of Chinese Academy of Sciences, Beijing 100049, China*

Xueming Yang − *State Key Laboratory of Chemical Reaction Dynamics, Dalian Institute of Chemical Physics, Chinese Academy of Sciences, Dalian 116023, China; University of Chinese Academy of Sciences, Beijing 100049, China; Institute of Advanced Science Facilities, Shenzhen 518107, China;* orcid.org/0000-0001-6684-9187

Complete contact information is available at: https://pubs.acs.org/10.1021/jacs.5c20067

Author Contributions

[#]H.W., Z.L., and H.J. contributed equally. All authors have approved the final version of the manuscript.

Notes

The authors declare no competing financial interest.

■ ACKNOWLEDGMENTS

We acknowledge the financial support from the National Key R&D Program of China (2022YFC3400500, 2025YFA1309300, and 2021ZD0203900), the National Natural Science Foundation of China (22525406, 22574159, 81821005, 92253303, U23A20108, 82341017, 22337004, and 22377089), the Strategic Priority Research Program of the Chinese Academy of Sciences (XDB0970100), the Science and Technology Commission of Shanghai Municipality (YDZX20233100004032), Shandong Laboratory Program (SYS202205), Zhongshan Institute for Drug Discovery (ZIDD202302), and Major Program of Guangzhou National Laboratory (GZNL2023A02012). We thank the staff members of the Large-scale Protein Preparation System (https://cstr.cn/31129.02.NFPS.LSPS) at the National Facility for Protein Science in Shanghai (https://cstr.cn/31129.02.NFPS), for providing technical support and assistance in data collection and analysis, the Shanghai Synchrotron Radiation Facility of BL02U1 (https://cstr.cn/31124.02.SSRF.BL02U1) and BL18U1 (http://e-ssrf.sari.ac.cn/beamlines/l18u1/) for crystallography data collection, and the technological support and assistance of the Biological Mass Spectrometry System (https://cstr.cn/31127.02.DCLS.ESBMS) at the Dalian Coherent Light Source (https://cstr.cn/31127.02.DCLS).

REFERENCES

(1) Moore, A. R.; Rosenberg, S. C.; McCormick, F.; Malek, S. RAS-targeted therapies: is the undruggable drugged? *Nat. Rev. Drug Discovery* **2020**, *19* (8), 533−552.

(2) Huang, L.; Guo, Z.; Wang, F.; Fu, L. KRAS mutation: from undruggable to druggable in cancer. *Signal. Transduct. Target. Ther.* **2021**, *6* (1), 386.

(3) Cancer Genome Atlas Research, N. Comprehensive molecular characterization of gastric adenocarcinoma. *Nature* **2014**, *513* (7517), 202−209. Kakiuchi, M.; Nishizawa, T.; Ueda, H.; Gotoh, K.; Tanaka, A.; Hayashi, A.; Yamamoto, S.; Tatsuno, K.; Katoh, H.; Watanabe, Y.; et al. Recurrent gain-of-function mutations of RHOA in diffuse-type gastric carcinoma. *Nat. Genet.* **2014**, *46* (6), 583−587. Wang, K.; Yuen, S. T.; Xu, J.; Lee, S. P.; Yan, H. H.; Shi, S. T.; Siu, H. C.; Deng, S.; Chu, K. M.; Law, S.; et al. Whole-genome sequencing and comprehensive molecular profiling identify new driver mutations in gastric cancer. *Nat. Genet.* **2014**, *46* (6), 573−582.

(4) Cherfils, J.; Zeghouf, M. Regulation of small GTPases by GEFs, GAPs, and GDIs. *Physiol. Rev.* **2013**, *93* (1), 269−309.

(5) Rossman, K. L.; Der, C. J.; Sondek, J. GEF means go: turning on RHO GTPases with guanine nucleotide-exchange factors. *Nat. Rev. Mol. Cell Biol.* **2005**, *6* (2), 167−180.

(6) Bos, J. L.; Rehmann, H.; Wittinghofer, A. GEFs and GAPs: critical elements in the control of small G proteins. *Cell* **2007**, *129* (5), 865−877.

(7) Garcia-Mata, R.; Boulter, E.; Burridge, K. The 'invisible hand': regulation of RHO GTPases by RHOGDIs. *Nat. Rev. Mol. Cell Biol.* **2011**, *12* (8), 493−504.

(8) Wei, Y.; Zhang, Y.; Derewenda, U.; Liu, X.; Minor, W.; Nakamoto, R. K.; Somlyo, A. V.; Somlyo, A. P.; Derewenda, Z. S. Crystal structure of RhoA-GDP and its functional implications. *Nat. Struct. Biol.* **1997**, *4* (9), 699−703.

(9) Ihara, K.; Muraguchi, S.; Kato, M.; Shimizu, T.; Shirakawa, M.; Kuroda, S.; Kaibuchi, K.; Hakoshima, T. Crystal structure of human RhoA in a dominantly active form complexed with a GTP analogue. *J. Biol. Chem.* **1998**, *273* (16), 9656−9666.

(10) Zhang, H.; Schaefer, A.; Wang, Y.; Hodge, R. G.; Blake, D. R.; Diehl, J. N.; Papageorge, A. G.; Stachler, M. D.; Liao, J.; Zhou, J.; et al. Gain-of-Function RHOA Mutations Promote Focal Adhesion Kinase Activation and Dependency in Diffuse Gastric Cancer. *Cancer Discovery* **2020**, *10* (2), 288−305.

(11) Kumagai, S.; Togashi, Y.; Sakai, C.; Kawazoe, A.; Kawazu, M.; Ueno, T.; Sato, E.; Kuwata, T.; Kinoshita, T.; Yamamoto, M.; Nomura, S.; Tsukamoto, T.; Mano, H.; Shitara, K.; Nishikawa, H.; et al. An Oncogenic Alteration Creates a Microenvironment that Promotes Tumor Progression by Conferring a Metabolic Advantage to Regulatory T Cells. *Immunity* **2020**, *53* (1), 187−203.

(12) Liu, J.; Li, S.; Chen, S.; Chen, S.; Geng, Q.; Xu, D. c-Met-dependent phosphorylation of RhoA plays a key role in gastric cancer tumorigenesis. *J. Pathol.* **2019**, *249* (1), 126−136.

(13) Hodge, R. G.; Ridley, A. J. Regulating Rho GTPases and their regulators. *Nat. Rev. Mol. Cell Biol.* **2016**, *17* (8), 496−510.

(14) Lawrence, S. A. S.; Dolan, A.; Miller, M. M.; Robinson, C. V. Membrane Protein Complexity Revealed Through Native Mass Spectrometry. *Annu. Rev. Biochem.* **2025**, *94* (1), 111−135.

(15) Zhou, M.; Lantz, C.; Brown, K. A.; Ge, Y.; Paša-Tolić, L.; Loo, J. A.; Lermyte, F. Higher-order structural characterisation of native proteins and complexes by top-down mass spectrometry. *Chem. Sci.* **2020**, *11* (48), 12918−12936.

(16) Shaw, J. B.; Li, W.; Holden, D. D.; Zhang, Y.; Griep-Raming, J.; Fellers, R. T.; Early, B. P.; Thomas, P. M.; Kelleher, N. L.; Brodbelt, J. S. Complete protein characterization using top-down mass spectrometry and ultraviolet photodissociation. *J. Am. Chem. Soc.* **2013**, *135* (34), 12646−12651.

(17) Cammarata, M. B.; Schardon, C. L.; Mehaffey, M. R.; Rosenberg, J.; Singleton, J.; Fast, W.; Brodbelt, J. S. Impact of G12 Mutations on the Structure of K-Ras Probed by Ultraviolet Photodissociation Mass Spectrometry. *J. Am. Chem. Soc.* **2016**, *138* (40), 13187−13196.

(18) Luo, P.; Liu, Z.; Lai, C.; Jin, Z.; Wang, M.; Zhao, H.; Liu, Y.; Zhang, W.; Wang, X.; Xiao, C.; et al. Time-Resolved Ultraviolet Photodissociation Mass Spectrometry Probes the Mutation-Induced Alterations in Protein Stability and Unfolding Dynamics. *J. Am. Chem. Soc.* **2024**, *146* (13), 8832−8838.

(19) Li, J.; Santambrogio, C.; Brocca, S.; Rossetti, G.; Carloni, P.; Grandori, R. Conformational effects in protein electrospray-ionization mass spectrometry. *Mass Spectrom. Rev.* **2016**, *35* (1), 111−122.

(20) Moghadamchargari, Z.; Huddleston, J.; Shirzadeh, M.; Zheng, X.; Clemmer, D. E.; M. Raushel, F.; Russell, D. H.; Laganowsky, A. Intrinsic GTPase Activity of K-RAS Monitored by Native Mass Spectrometry. *Biochemistry* **2019**, *58* (31), 3396−3405.

(21) John, J.; Rensland, H.; Schlichting, I.; Vetter, I.; Borasio, G. D.; Goody, R. S.; Wittinghofer, A. Kinetic and structural analysis of the Mg(2+)-binding site of the guanine nucleotide-binding protein p21H-ras. *J. Biol. Chem.* **1993**, *268* (2), 923−929.

(22) Mehaffey, M. R.; Schardon, C. L.; Novelli, E. T.; Cammarata, M. B.; Webb, L. J.; Fast, W.; Brodbelt, J. S. Investigation of GTP-dependent dimerization of G12X K-Ras variants using ultraviolet photodissociation mass spectrometry. *Chem. Sci.* **2019**, *10* (34), 8025−8034. Brodbelt, J. S.; Morrison, L. J.; Santos, I. Ultraviolet Photodissociation Mass Spectrometry for Analysis of Biological Molecules. *Chem. Rev.* **2020**, *120* (7), 3328−3380.

(23) Macias, L. A.; Sipe, S. N.; Santos, I. C.; Bashyal, A.; Mehaffey, M. R.; Brodbelt, J. S. Influence of Primary Structure on Fragmentation of Native-Like Proteins by Ultraviolet Photodissociation. *J. Am. Soc. Mass Spectrom.* **2021**, *32* (12), 2860−2873.

(24) Lin, Y.; Lu, S.; Zhang, J.; Zheng, Y. Structure of an inactive conformation of GTP-bound RhoA GTPase. *Structure* **2021**, *29* (6), 553−563.

(25) Jiang, H.; Zu, S.; Lu, Y.; Sun, Z.; Adeerjiang, A.; Guo, Q.; Zhang, H.; Dong, C.; Wu, Q.; Ding, H.; et al. A RhoA structure with switch II flipped outward revealed the conformational dynamics of switch II region. *J. Struct. Biol.* **2023**, *215* (2), No. 107942.

(26) Lin, Y.; Ramelot, T. A.; Senyuz, S.; Gursoy, A.; Jang, H.; Nussinov, R.; Keskin, O.; Zheng, Y. Tumor-derived RHOA mutants interact with effectors in the GDP-bound state. *Nat. Commun.* **2024**, *15* (1), 7176.

(27) Ostrem, J. M.; Peters, U.; Sos, M. L.; Wells, J. A.; Shokat, K. M. K-Ras(G12C) inhibitors allosterically control GTP affinity and effector interactions. *Nature* **2013**, *503* (7477), 548−551. Canon, J.; Rex, K.; Saiki, A. Y.; Mohr, C.; Cooke, K.; Bagal, D.; Gaida, K.; Holt, T.; Knutson, C. G.; Koppada, N.; et al. The clinical KRAS(G12C) inhibitor AMG 510 drives anti-tumour immunity. *Nature* **2019**, *575* (7781), 217−223. Fell, J. B.; Fischer, J. P.; Baer, B. R.; Blake, J. F.; Bouhana, K.; Briere, D. M.; Brown, K. D.; Burgess, L. E.; Burns, A. C.; Burkard, M. R.; et al. Identification of the Clinical Development Candidate MRTX849, a Covalent KRAS(G12C) Inhibitor for the Treatment of Cancer. *J. Med. Chem.* **2020**, *63* (13), 6679−6693.

(28) Kessler, D.; Bergner, A.; Böttcher, J.; Fischer, G.; Döbel, S.; Hinkel, M.; Müllauer, B.; Weiss-Puxbaum, A.; McConnell, D. B. Drugging all RAS isoforms with one pocket. *Future Med. Chem.* **2020**, *12* (21), 1911−1923.

(29) Shang, X.; Marchioni, F.; Sipes, N.; Evelyn, C. R.; Jerabek-Willemsen, M.; Duhr, S.; Seibel, W.; Wortman, M.; Zheng, Y. Rational design of small molecule inhibitors targeting RhoA subfamily Rho GTPases. *Chem. Biol.* **2012**, *19* (6), 699−710.

(30) Ostrem, J. M.; Shokat, K. M. Direct small-molecule inhibitors of KRAS: from structural insights to mechanism-based design. *Nat. Rev. Drug Discovery* **2016**, *15* (11), 771−785.

(31) Gao, J.; Ma, R.; Wang, W.; Wang, N.; Sasaki, R.; Snyderman, D.; Wu, J.; Ruan, K. Automated NMR fragment based screening identified a novel interface blocker to the LARG/RhoA complex. *PLoS One* **2014**, *9* (2), No. e88098. Chen, M.; Pan, H.; Sun, L.; Shi, P.; Zhang, Y.; Li, L.; Huang, Y.; Chen, J.; Jiang, P.; Fang, X.; et al. Structure and regulation of human epithelial cell transforming 2 protein. *Proc. Natl. Acad. Sci. U. S. A.* **2020**, *117* (2), 1027−1035.

(32) Ellerbroek, S. M.; Wennerberg, K.; Burridge, K. Serine phosphorylation negatively regulates RhoA in vivo. *J. Biol. Chem.*

https://doi.org/10.1021/jacs.5c20067
J. Am. Chem. Soc. 2026, 148, 11709−11718

2003, *278* (21), 19023−19031. Kim, J. G.; Mahmud, S.; Min, J. K.; Lee, Y. B.; Kim, H.; Kang, D. C.; Park, H. S.; Seong, J.; Park, J. B. RhoA GTPase phosphorylated at tyrosine 42 by src kinase binds to *β*-catenin and contributes transcriptional regulation of vimentin upon Wnt3A. *Redox Biol.* **2021**, *40*, No. 101842.

(33) Chen, X.; Ji, S.; Liu, Z.; Yuan, X.; Xu, C.; Qi, R.; He, A.; Zhao, H.; Song, H.; Xiao, C.; Gao, W.; Chen, P. R.; Luo, R.; Li, P.; Wang, F.; Yang, X.; Tian, R.; et al. Motif-dependent immune co-receptor interactome profiling by photoaffinity chemical proteomics. *Cell Chem. Biol.* **2022**, *29* (6), 1024−1036.